INTERPRETATION OF THE UNPRECEDENTEDLY LONG-LIVED HIGH-ENERGY EMISSION OF GRB 130427A

RUO-YU LIU[1,2,4,7], XIANG-YU WANG[1,4], AND XUE-FENG WU[3,5,6]
[1] School of Astronomy and Space Science, Nanjing University, Nanjing 210093, China
[2] Max-Planck-Institut für Kernphysik, D-69117 Heidelberg, Germany
[3] Purple Mountain Observatory, Chinese Academy of Sciences, Nanjing 210008, China
[4] Key laboratory of Modern Astronomy and Astrophysics (Nanjing University), Ministry of Education, Nanjing 210093, China
[5] Chinese Center for Antarctic Astronomy, Nanjing 210008, China
[6] Joint Center for Particle, Nuclear Physics and Cosmology, Nanjing University-Purple Mountain Observatory, Nanjing 210008, China

ABSTRACT

High-energy photons (>100 MeV) are detected by the *Fermi*/Large Area Telescope from GRB 130427A up to almost one day after the burst, with an extra hard spectral component discovered in the high-energy afterglow. We show that this hard spectral component arises from afterglow synchrotron self-Compton (SSC) emission. This scenario can explain the origin of >10 GeV photons detected up to $\sim$30,000 s after the burst, which would be difficult to explain via synchrotron radiation due to the limited maximum synchrotron photon energy. The lower energy multi-wavelength afterglow data can be fitted simultaneously by the afterglow synchrotron emission. The implication of detecting the SSC emission for the circumburst environment is discussed.

1. INTRODUCTION

The extended high-energy emission detected by *Fermi*/Large Area Telescope (LAT) is widely believed to arise from the electrons accelerated in the external forward shock via the synchrotron radiation (e.g., Kumar & Barniol Duran 2009, 2010). However, the maximum photon energy in this scenario is limited to be $\varepsilon_{\gamma,\max} = 50\,\Gamma$ MeV, where 50 MeV is the maximum synchrotron photon in the rest frame of the shock and Γ is the bulk Lorentz factor of the shock, which is usually $\lesssim$300 at $\sim$100 s after the trigger (e.g., Piran & Nakar 2010; Barniol Duran & Kumar 2011). Thus, the detection of >10 GeV photons after 100 s poses a challenge for the synchrotron emission scenario (Piran & Nakar 2010; Sagi & Nakar 2012). Considering the above difficulty, Wang et al. (2013) recently proposed that the afterglow synchrotron self-Compton (SSC) emission or the external inverse-Compton of the central X-ray emission (Wang et al. 2006) is likely responsible for the late-time >10 GeV photons seen in some LAT gamma-ray bursts (GRBs).

GRB 130427A triggered the *Fermi*/GBM with a fluence of 2×10^3 erg cm^{-2} in 10–1000 keV within a duration of $T_{90} = 138$ s (von Kienlin 2013). It was later localized at $z \simeq 0.34$ (Flores et al. 2013; Levan et al. 2013; Xu et al. 2013b), implying an isotropic energy of 7.8×10^{53} erg (Kann & Schulze 2013). Unprecedentedly, >100 MeV emissions are detected well beyond the prompt emission phase up to about one day after the burst, including 15 photons >10 GeV detected up to $\sim$30,000 s and 1 95.3 GeV photon that arrived at 243 s after the trigger (Zhu et al. 2013; Tam et al. 2013). It was suggested that these late-time high-energy photons may arise from inverse-Compton processes (Fan et al. 2013; Wang et al. 2013). Further evidence comes from the presence of a hard spectral component (the photon index $\Gamma_{\rm ph} = -1.4 \pm 0.1$) above 2.5 ± 1.1 GeV (Tam et al. 2013) in the late afterglow, which has

signatures consistent with the prediction of the afterglow SSC emission (Zhang & Mészáros 2001; Sari & Esin 2001; Zou et al. 2009). In this Letter, we will verify this possibility by modeling the multi-band (from radio to GeV bands) data of this burst. Hereafter, we denote by Q_x the value of the quantity Q in units of 10^x.

2. A BRIEF OVERVIEW OF THE MODEL

In the standard synchrotron afterglow spectrum, there are three break frequencies, ν_a, ν_m, and ν_c, which are caused by synchrotron self-absorption, electron injection, and electron cooling, respectively. According to, for example, Sari et al. (1998) and Wijers & Galama (1999), these three characteristic frequencies are given by

$$\nu_{\rm m} = 1.1 \times 10^{18}\, f^2(p)\epsilon_{e,-1}^2 E_{54}^{1/2}\epsilon_{\rm B,-5}^{1/2}(1+z)^{1/2}T^{-3/2}\ {\rm Hz}, \quad (1)$$

$$\nu_{\rm c} = 1.1\times 10^{17}\, E_{54}^{-1/2}n_0^{-1}\epsilon_{\rm B,-5}^{-3/2}\left(\frac{1+Y}{100}\right)^{-2}(1+z)^{-1/2}T^{-1/2}\ {\rm Hz}, \quad (2)$$

and

$$\nu_a = 2.7 \times 10^{10}\, f^{-1}(p)E_{54}^{1/5}\epsilon_{e,-1}^{-1}\epsilon_{\rm B,-5}^{1/5}n_0^{3/5}(1+z)^{-1}, \quad (3)$$

in the case that $\nu_a < \nu_m < \nu_c$, which is usually true under typical parameter values. In the above three equations, T is the time in the observer's frame since the trigger time z is the redshift of the burst $f(p) = 6(p-2)/(p-1)$, with p being the electron index, E the isotropic kinetic energy of the GRB outflow, and n the number density of the circumburst medium. For an interstellar medium (ISM) circumburst environment, n is constant, while for a stellar wind circumburst environment, it is inversely proportional to the square of the shock radius. $\epsilon_{\rm e}$ and $\epsilon_{\rm B}$ are the equipartition factors for the energy in electrons and magnetic field in the shock, respectively. In the expression

of ν_c, Y is the Compton parameter evaluating the effect of SSC cooling on the synchrotron spectrum. In the Thomson scattering limit, $Y = Y_0 \simeq (\epsilon_e/\epsilon_B)^{1/4-p}(\nu_m/\nu_{c,\mathrm{syn}})^{p-2/2(4-p)}$ (Sari & Esin 2001) if $Y \gg 1$, where $\nu_{c,\mathrm{syn}}$ is obtained by considering only the synchrotron cooling.

The time-integrated spectrum of high-energy emission from GRB 130427A can be modeled by a broken power law with a soft component ($\Gamma_{\mathrm{ph}} = 2.3 \pm 0.1$) below the break energy $E_b = 2.5 \pm 1.1$ GeV and a hard component ($\Gamma_{\mathrm{ph}} = 1.4 \pm 0.1$) above E_b (Tam et al. 2013). It is natural to assume that synchrotron emission is dominant below E_b while the SSC emission is dominant above E_b. Like Tam et al. (2013), we assume $p = 2.2$ in the following analysis. Thus, the synchrotron flux at $h\nu_c < 100\,\mathrm{MeV} \leqslant h\nu_{\mathrm{LAT}} < E_b$ is given by

$$F_\nu(100\,\mathrm{MeV}) = 7.0\, E_{54}^{1.05}\epsilon_{e,-1}^{1.2}\epsilon_{B,-5}^{0.05}(1+z)^{1.05}$$
$$\times D_{L,28}^{-2}T^{-1.15}\left(\frac{h\nu}{100\,\mathrm{MeV}}\right)^{-1.1} \mu\mathrm{Jy}, \quad (4)$$

where D_L is the luminosity distance. Here we neglect the inverse-Compton cooling for the electrons that radiate high-energy gamma-ray emission due to the deep Klein–Nishina (KN) scattering effect (Wang et al. 2010; Liu & Wang 2011). The emission above E_b can be interpreted as the SSC emission in the regime of $h\nu_m^{\mathrm{ssc}} < h\nu_{\mathrm{LAT}} < h\nu_c^{\mathrm{ssc}}$, where ν_m^{ssc} and ν_c^{ssc} are the corresponding break frequencies in the SSC spectrum. The SSC flux is given by (Sari & Esin 2001)

$$F_\nu(10\,\mathrm{GeV}) = 5.6 \times 10^{-3} E_{54}^{1.7}n_0^{1.1}\epsilon_{e,-1}^{2.4}\epsilon_{B,-5}^{0.8}(1+z)^{1.5}$$
$$\times D_{L,28}^{-2}T^{-1.1}\left(\frac{h\nu}{10\,\mathrm{GeV}}\right)^{-0.6} \mu\mathrm{Jy}. \quad (5)$$

Lower energy emission is produced by the forward shock synchrotron radiation. X-ray observation frequency is usually also in the fast cooling regime, i.e., $\nu_m < \nu_c < \nu_X$. However, the KN suppression effect is not as important as in the case of >100 MeV emission, so we need to carefully consider the effect of SSC cooling on the synchrotron spectrum. Thus, we have

$$F_\nu(10\,\mathrm{keV}) = 17\, E_{54}^{1.05}\epsilon_{e,-1}^{1.2}\epsilon_{B,-5}^{0.05}\left[\frac{1+Y(10\,\mathrm{keV})}{10}\right]^{-1}$$
$$\times (1+z)^{1.05}D_{L,28}^{-2}T^{-1.15}\left(\frac{h\nu}{10\,\mathrm{keV}}\right)^{-1.1} \mathrm{mJy}. \quad (6)$$

Here $Y(10\,\mathrm{keV}) = f_{\mathrm{KN}}Y_0$ with $Y_0 = U_{\mathrm{syn}}/U_B = 110\, E_{54}^{0.056}n_0^{0.056}\epsilon_{e,-1}^{0.67}\epsilon_{B,-5}^{-0.44}(1+z)^{0.056}T^{-0.056}$ being the Compton parameter in the Thomson scattering limit as mentioned above, where U_{syn} and U_B are the energy density of synchrotron radiation field and magnetic field, respectively. The factor f_{KN} considers the KN effect on the electrons that emit 10 keV photons by synchrotron radiation. In the Thomson scattering regime $f_{\mathrm{KN}} = 1$, while in the deep KN scattering regime $f_{\mathrm{KN}} \to 0$.

The KN effect will intervene in the inverse Compton cooling if the energy of the incident photon exceeds the rest energy of the scattering electron in its rest frame, i.e., $\gamma_e h\nu_{\mathrm{KN}}(1+z)/\Gamma \geqslant m_e c^2$, where γ_e is the Lorentz factor of the electron in the comoving frame of the emitting region and ν_{KN} is the critical frequency of the incidence photon measured in the observer's frame. If the energy of a photon is larger than $h\nu_{\mathrm{KN}}$, the scatter will enter the KN regime with a suppressed cross section. The

Lorentz factor of the electron emitting X-ray photons can be given by $\gamma_{10\,\mathrm{keV}} = ((2\pi m_e c\nu_X(1+z))/\Gamma eB)^{1/2}$ and thus

$$\nu_{\mathrm{KN},10\,\mathrm{keV}} = 2.8 \times 10^{18} E_{54}^{1/4}\epsilon_{B,-5}^{1/4}(1+z)^{-3/4}$$
$$\times \left(\frac{h\nu_X}{10\,\mathrm{keV}}\right)^{1/2} T^{-3/4}. \quad (7)$$

As $\nu_{\mathrm{KN}} \propto T^{-3/4}$, the KN suppression effect becomes more and more important at later time. As a rough estimate, f_{KN} can be given by

$$f_{\mathrm{KN}} = \frac{U_{\mathrm{syn}}(\nu < \nu_{\mathrm{KN}})}{U_{\mathrm{syn}}}$$
$$\simeq \begin{cases} 0.06\left(\frac{\nu_m}{\nu_c}\right)^{0.4}\left(\frac{\nu_{\mathrm{KN}}}{\nu_m}\right)^{4/3} & \nu_{\mathrm{KN}} < \nu_m, \\ 0.2\left(\frac{\nu_{\mathrm{KN}}}{\nu_c}\right)^{0.4} & \nu_m < \nu_{\mathrm{KN}} < \nu_c. \\ 1 - 0.8\left(\frac{\nu_{\mathrm{KN}}}{\nu_c}\right)^{-0.1} & \nu_c < \nu_{\mathrm{KN}} \end{cases} \quad (8)$$

In a broad parameter space, we find $\nu_m < \nu_{\mathrm{KN}} < \nu_c$, leading to $f_{\mathrm{KN}} \simeq 0.1E_{54}^{0.3}n_0^{0.4}\epsilon_{B,-5}^{0.7}(1+z)^{0.1}[(1+Y(10\,\mathrm{keV}))/10]^{0.8}(h\nu/10\,\mathrm{keV})^{0.2}T^{-0.1}$.

Optical emission is typically in the frequency regime $\nu_m < \nu_{\mathrm{Op}} < \nu_c$, so the flux is given by

$$F_\nu(R\,\mathrm{band}) = 1.3\, E_{54}^{1.3}n_0^{0.5}\epsilon_{e,-1}^{1.2}\epsilon_{B,-5}^{0.8}(1+z)^{1.3}$$
$$\times D_{L,28}^{-2}T^{-0.9}\left(\frac{\nu}{4.56 \times 10^{14}\,\mathrm{Hz}}\right)^{-0.6} \mathrm{Jy}. \quad (9)$$

The radio observation frequency could lie in the regime $\nu_a < \nu_{\mathrm{Ra}} < \nu_m$ or $\nu_{\mathrm{Ra}} < \nu_a < \nu_m$. In the former case,

$$F_\nu(5\,\mathrm{GHz}) = 20\, E_{54}^{5/6}n_0^{1/2}\epsilon_{e,-1}^{-2/3}\epsilon_{B,-5}^{1/3}(1+z)^{5/6}$$
$$\times D_{L,28}^{-2}T^{1/2}\left(\frac{\nu}{5\,\mathrm{GHz}}\right)^{1/3} \mu\mathrm{Jy}, \quad (10)$$

while in the latter case,

$$F_\nu(5\,\mathrm{GHz}) = 1.3\, E_{54}^{1/2}n_0^{-1/2}\epsilon_{e,-1}(1+z)^{5/2}$$
$$\times D_{L,28}^{-2}T^{1/2}\left(\frac{\nu}{5\,\mathrm{GHz}}\right)^2 \mu\mathrm{Jy}. \quad (11)$$

We note that, in previous works, modeling of the multi-band light curves of LAT-detected GRBs usually result in a low circumburst density $<10^{-2}$ cm^{-3} (e.g., Cenko et al. 2011; Liu & Wang 2011; He et al. 2011). In a low-density environment, SSC flux would be severely suppressed. Here we point out that the low-density result is mainly caused by neglecting the KN effect in modeling the X-ray afterglows. We now briefly show that considering the KN effect in X-ray afterglow can dramatically change the inferred density.

Usually >10 GeV data are not available, and only >100 MeV, X-ray, optical, and radio data are used in the multi-band light curve fit. Thus from Equations (4), (6), (9), and (10) or (11) we get four independent constraints on four undetermined parameters, namely E, n, ϵ_e, and ϵ_B (note that $p = 2.2$ is fixed). Thus we can fully determine these parameters by solving these

equations. In the case that KN effect is not considered in X-ray emission, i.e., $f_{KN} = 1$, we get

$$\begin{cases} E \simeq C_{LAT}^{0.74} C_X^{0.45} C_{Op}^{-0.59} C_{Ra}^{0.64} \\ n \simeq C_{LAT}^{0.28} C_X^{-2.26} C_{Op}^{1.09} C_{Ra}^{0.66} \\ \epsilon_e \simeq C_{LAT}^{0.26} C_X^{-0.45} C_{Op}^{0.48} C_{Ra}^{-0.53} \\ \epsilon_B \simeq C_{LAT}^{-1.77} C_X^{1.35} C_{Op}^{0.80} C_{Ra}^{-0.65}. \end{cases} \quad (12)$$

Here we adopt the case that $\nu_a < \nu < \nu_m$ for radio flux as an example. C_{LAT}, C_X, C_{Op}, and C_{Ra} are constants related to data used to normalize the flux in LAT, X-ray, optical, and radio band, respectively.

When considering the KN effect in X-ray, as long as $Y = f_{KN} Y_0 \gtrsim 1$, we can approximately replace the C_X by $C_X f_{KN}$ in the above equation set and we then get

$$\begin{cases} E = f_{KN}^{0.45} \hat{E} \\ n = f_{KN}^{-2.26} \hat{n} \\ \epsilon_e = f_{KN}^{-0.45} \hat{\epsilon}_e \\ \epsilon_B = f_{KN}^{1.35} \hat{\epsilon}_B. \end{cases} \quad (13)$$

Here we denote the parameters without considering the KN effect on X-ray emission by hatted characters. If $f_{KN} Y_0 \ll 1$, f_{KN} should be replaced by $(1 + Y_0)^{-1}$ in the above equation set. Since $f_{KN} < 1$, considering the KN effect in X-ray emission will significantly increase the inferred ISM density. Substituting Equation (13) into Equation (5), we find $F_{\nu,IC} \simeq f_{KN}^{-1.7} \hat{F}_{\nu,IC}$, so the SSC flux can be significantly increased as well.

Here we point out that Equation (8) underestimates the value of f_{KN} because the scattering cross section in the KN regime is approximated as being zero. In our numerical code, we calculate f_{KN} as

$$f_{KN} = \frac{\int_0^{\nu_{KN}} F_\nu d\nu + \int_{\nu_{KN}}^{\infty} [2 \ln(2 \gamma_e h\nu / \Gamma m_e c^2) + 1] \left(\frac{\nu}{\nu_{KN}}\right)^{-1} F_\nu d\nu}{\int_0^{\infty} F_\nu d\nu}, \quad (14)$$

where the expression before F_ν in the second integration on the numerator accounts for the correction to the scattering cross section above ν_{KN}.

3. FITTING OF THE MULTI-BAND LIGHT CURVE DATA

There are abundant observational data of the multi-band light curves of GRB 130427A. The extended high-energy emission in the energy range 0.1–2 GeV and 2–100 GeV shows a power-law decay with slopes of $\alpha_1 = 1.1 \pm 0.1$ and $\alpha_2 = 1.0 \pm 0.1$, respectively (Tam et al. 2013). Therefore we adopt the ISM density profile for the circumburst environment because in the wind environment the late-time SSC flux would decrease much faster than the observed one.[8]

According to the *Fermi*/LAT spectral data shown in Tam et al. (2013), the 0.1–2 GeV flux is dominated by the synchrotron component. Requiring the synchrotron flux to be 10^{-4} photons cm^{-2} s^{-1} at 300 s, we obtain

$$E_{54}^{1.05} \epsilon_{e,-1}^{1.2} \epsilon_{B,-5}^{0.05} = 1.5. \quad (15)$$

By requiring the SSC flux to be 3×10^{-7} photons cm^{-2} s^{-1} at 5000 s in 2–100 GeV, we obtain

$$E_{54}^{1.7} \epsilon_{e,-1}^{2.4} \epsilon_{B,-5}^{0.8} n_0^{1.1} = 20. \quad (16)$$

The X-Ray Telescope data show that the X-ray flux decays with a slope of -1.2 since 421 s after the trigger, then breaks at 53.4 ks to a steeper slope of -1.8 (Evans et al. 2013), and after $\sim$1 day the light curve becomes shallower again with a slope of -1.3. The first slope is consistent with the decay of the synchrotron flux when the observation frequency is above the cooling frequency, i.e., $\nu_X > \nu_c$. To explain the second slope, we introduce a jet break around 53.4 ks. The late-time shallower decay could be due to the KN suppression effect which becomes more and more important at later times. Since the KN effect is not easy to express accurately in an analytical way, we include it in the numerical modeling.

The optical flux decreases slowly at early time with a slope of -0.8 (Laskar et al. 2013), which is consistent with the decay slope of synchrotron emission in the frequency regime $\nu_m < \nu_{opt} < \nu_c$. The light curve becomes obviously steeper after $\sim$0.3 day with a slope of -1.35 (Laskar et al. 2013) and then a flattening shows up at $\sim$10 days after the trigger (Trotter et al. 2013). The steepening in the light curve can be ascribed to the jet break as well. Although the jet break usually results in a steeper slope than -1.35, we note that there is an emerging supernova component (Xu et al. 2013a), so this shallow slope could be caused by the superposition of the fast decaying synchrotron afterglow component and the supernova component. Since the R-band flux is about 1 mJy at $\sim$30 ks, we have

$$E_{54}^{1.3} \epsilon_{e,-1}^{1.2} \epsilon_{B,-5}^{0.8} n_0^{0.5} = 1.8. \quad (17)$$

The radio data starts from $\sim$0.67 day after the trigger (Laskar et al. 2013), which is around the assumed jet break time. The observed 5 GHz flux at 0.67 day and 2 days after the trigger are comparable, and decreases by a factor of a few at 4.7 days. This decay can be ascribed to the jet break. Higher frequency observations such as 20 GHz, 36 GHz start later and show a decaying light curve from the beginning. By requiring that the synchrotron flux at 5 GHz flux be 2 mJy at 0.67 day, we get

$$E_{54}^{0.5} \epsilon_{e,-1} n_0^{-0.5} = 0.9. \quad (18)$$

The early radio emission can be also attributed to the reverse shock emission, as suggested by Laskar et al. (2013).[9] Then we will require that the flux produced by the forward shock is below the observed flux. This is possible in the framework of the decaying micro-turbulence magnetic field scenario (Lemoine et al. 2013; Wang et al. 2013), since the radio-emitting electrons radiate in a weaker magnetic field region.

As we can see, the early- and late-time LAT observations and the optical and the radio observations already provide four independent constraints on four parameters (i.e., E, n, ϵ_e, and ϵ_B). Since the X-ray observation can in principle put another constraint independently, the system of equations is overdetermined. Finding a solution for the overdetermined system of equations supports the validity of our model.

---

[8] In the ISM medium, $\nu_{m,IC} \propto T^{-9/4}$, $F_{\nu m,IC} \propto T^{1/4}$, and $F_\nu = F_{\nu m,IC}(\nu/\nu_m)^{-(p-1)/2} \propto T^{(11-9p)/8}$. In the wind medium, $\nu_{m,IC} \propto t^{-2}$ and $F_{\nu m,IC} \propto t^{-1}$, so $F_\nu = F_{\nu m,IC}(\nu/\nu_m)^{-(p-1)/2} \propto t^{-p}$.

[9] Introducing a reverse shock component helps to explain the observed soft radio spectrum ($F_\nu \propto \nu^\beta$ with $\beta < 0$) at 2 days and 4.7 days after the trigger time. On the other hand, we also note that radio observations during early time (e.g., <10 days after the trigger time) may suffer from the interstellar scintillation (Goodman 1997), so the observed flux and spectral index could be affected to some extent.
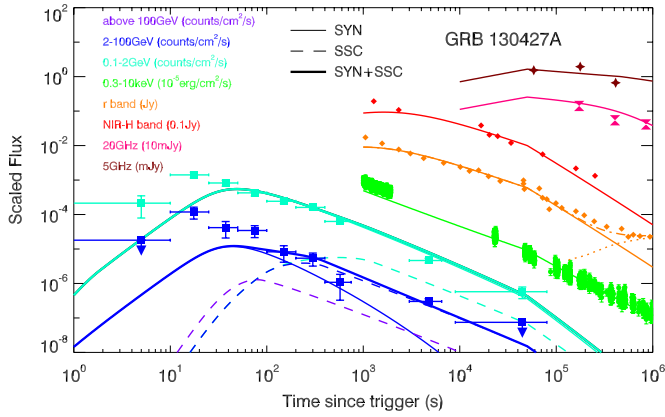
Figure 1. Fit of the multi-band light curves of GRB 130427A. For the high-energy emission, the thin solid lines represent the synchrotron flux, the dashed lines represent the SSC flux, and the thick solid lines represent the total flux. The orange dotted line represents the supernova component, which has the same shape as SN1998bw but with a flux normalized to the detected flux. The orange dotted line is the sum of the GRB afterglow component and the supernova component. The LAT data is taken from Tam et al. (2013). The X-ray data is taken from the Web site http://www.swift.ac.uk/xrt_curves. The optical, near-infrared data, and radio data are taken from Laskar et al. (2013). In this fit, we used the following parameter values: $E_k = 2 \times 10^{53}$ erg, $\epsilon_e = 0.6$, $\epsilon_B = 1.3 \times 10^{-5}$, $n = 1\,\mathrm{cm}^{-3}$, $p = 2.2$, and $\Gamma_0 = 200$. The jet break time is set at 0.65 day after the trigger time. The opening angle is $\theta_j = 7°$, corresponding to $E_{k,\mathrm{jet}} = 1.5 \times 10^{51}$ erg.

(A color version of this figure is available in the online journal.)

Figure 2. Fit of the spectrum of LAT emission at two different times. The dashed lines and the dash-dotted lines represent the synchrotron component and the SSC component respectively, and the solid lines represent the sum of them.

(A color version of this figure is available in the online journal.)

By solving the above four equations, we get $E_{54} \simeq 0.3$, $n_0 \simeq 6$, $\epsilon_{e,-1} \simeq 5$, and $\epsilon_{B,-5} \simeq 0.5$. Although the analytic solution and numerical solution may not conform each other perfectly, we can use these values as a guide, and fine-tune them to get a good global solution in our numerical code. We show the fitting of multi-band light curves in Figure 1. The final values of the parameters are not much different from the above values, as shown in the caption of the figure. We also present the light curve of >100 GeV SSC emission with a purple dashed line. It peaks around 100 s with a flux of 10^{-6} photons cm^{-2} s^{-1}. Given the LAT effective area of $\sim 10^4$ cm^{-2}, one may expect that LAT may detect one $\gtrsim$100 GeV photon in $\sim$100 s around the peak time, which is consistent with the detection of the 95.3 GeV photon at 243 s after the trigger time. Our model cannot explain the high energy emission during the prompt emission phase ($\lesssim$100 s), which is attributed to the internal dissipation origin (He et al. 2011; Liu & Wang 2011; Maxham et al. 2011). In the numerical modeling, we find that $f_{\mathrm{KN}}(10\,\mathrm{keV})$ gradually decreases from $\gtrsim$0.1 at 1000 s to $\sim$0.01 at 10^6 s. Figure 2 presents the fit of the time-integrated spectrum of LAT emission for the period of 138–750 s and 3000–80,000 s.

4. DISCUSSIONS

The extended, hard emission above a few GeV, seen in GRB 130427A, represents strong evidence of a SSC component in the forward shock emission. The appearance of the SSC component implies that the circumburst density should not be too low, in contrast to the result in the previous study that the circumburst density of LAT-detected bursts is on average lower than usual (Cenko et al. 2011). The inferred density in this work is of the same order of the typical ISM density in the galaxy disk where massive stars reside.

Recently, Laskar et al. (2013) modeled the low-energy afterglows of this GRB with a forward-reverse shock synchrotron
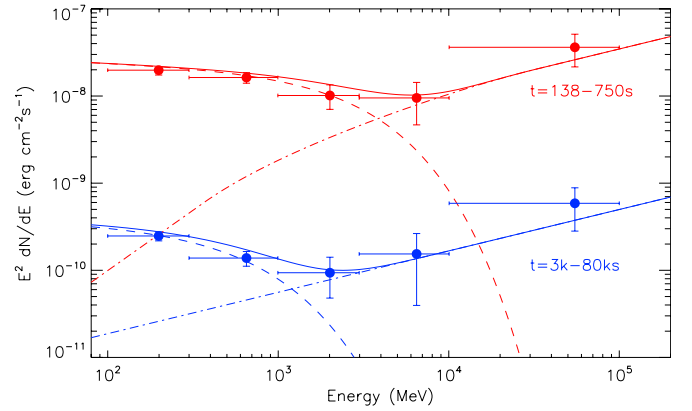
emission model. However, we find that their model predicts a synchrotron flux about one order of magnitude lower than the observed flux in the LAT energy range. To interpret the multi-band afterglow data including the LAT data, we proposed a forward shock synchrotron plus SSC emission scenario. We also find that an ISM environment is favored by the slow decay of 2–100 GeV flux, which is explained as the SSC origin.

REFERENCES

Barniol Duran, R., & Kumar, P. 2011, MNRAS, 412, 522
Cenko, S. B., Frail, D. A., Harrison, F. A., et al. 2011, ApJ, 732, 29
Evans, P. A., Page, K. L., Maselli, A., et al. 2013, GCN, 14502, 1
Fan, Y.-Z., Tam, P. H. T., Zhang, F.-W., et al. 2013, arXiv:1305.1261
Flores, H., Covino, S., Xu, D., et al. 2013, GCN, 14491, 1
Goodman, J. 1997, NewA, 2, 449
He, H. N., Wu, X. F., Toma, K., Wang, X. Y., & Mészáros, P. 2011, ApJ, 733, 22
Kann, D. A., & Schulze, S. 2013, GCN, 14580, 1
Kumar, P., & Barniol Duran, R. 2009, MNRAS, 400, L75
Kumar, P., & Barniol Duran, R. 2010, MNRAS, 409, 226
Laskar, T., Berger, E., Zauderer, B. A., et al. 2013, arXiv:1305.2453
Lemoine, M., Li, Z., & Wang, X.-Y. 2013, arXiv:1305.3689
Levan, A. J., Cenko, S. B., Perley, D. A., & Tanvir, N. R. 2013, GCN, 14455, 1
Liu, R. Y., & Wang, X. Y. 2011, ApJ, 730, 1
Maxham, A., Zhang, B.-B., & Zhang, B. 2011, MNRAS, 415, 77
Piran, T., & Nakar, E. 2010, ApJL, 718, L63
Sagi, E., & Nakar, E. 2012, ApJ, 749, 80
Sari, R., & Esin, A. A. 2001, ApJ, 548, 787
Sari, R., Piran, T., & Narayan, R. 1998, ApJL, 497, L17
Tam, P.-H. T., Tang, Q.-W., Hou, S., Liu, R.-Y., & Wang, X.-Y. 2013, ApJL, 771, L13
Trotter, A., Reichart, D., Haislip, J., et al. 2013, GCN, 14510, 1
von Kienlin, A. 2013, GCN, 14473, 1

Wang, X.-Y., He, H.-N., Li, Z., Wu, X.-F., & Dai, Z.-G. 2010, ApJ, 712, 1232
Wang, X.-Y., Li, Z., & Mészáros, P. 2006, ApJL, 641, L89
Wang, X.-Y., Liu, R.-Y., & Lemoine, M. 2013, ApJL, 771, L33
Wijers, R. A. M. J., & Galama, T. J. 1999, ApJ, 523, 177

Xu, D., de Ugarte Postigo, A., Leloudas, G., et al. 2013a, arXiv:1305.6832
Xu, D., de Ugarte Postigo, A., Schulze, S., et al. 2013b, GCN, 14478, 1
Zhang, B., & Mészáros, P. 2001, ApJ, 559, 110
Zhu, S., Racusin, J., Kocevski, D., et al. 2013, GCN, 14508, 1
Zou, Y.-C., Fan, Y.-Z., & Piran, T. 2009, MNRAS, 396, 1163